

Interpreting Adversarial Attacks and Defences using Architectures with Enhanced Interpretability

Akshay G Rao, Chandrashekar Lakshminarayanan & Arun Rajkumar

Department of Computer Science, Indian Institute of Technology Madras
akshaygrao@outlook.com, chandrashekar@cse.iitm.ac.in, arunr@cse.iitm.ac.in

Abstract

Adversarial attacks in deep learning represent a significant threat to the integrity and reliability of machine learning models. Adversarial training has been a popular defence technique against these adversarial attacks. In this work, we capitalize on a network architecture, namely Deep Linearly Gated Networks (DLGN), which has better interpretation capabilities than regular deep network architectures. Using this architecture, we interpret robust models trained using PGD adversarial training and compare them with standard training. Feature networks in DLGN act as feature extractors, making them the only medium through which an adversary can attack the model. We analyze the feature network of DLGN with fully connected layers with respect to properties like alignment of the hyperplanes, hyperplane relation with PCA, and sub-network overlap among classes and compare these properties between robust and standard models. We also consider this architecture having CNN layers wherein we qualitatively (using visualizations) and quantitatively contrast gating patterns between robust and standard models. We uncover insights into hyperplanes resembling principal components in PGD-AT and STD-TR models, with PGD-AT hyperplanes aligned farther from the data points. We use path activity analysis to show that PGD-AT models create diverse, non-overlapping active subnetworks across classes, preventing attack-induced gating overlaps. Our visualization ideas show the nature of representations learnt by PGD-AT and STD-TR models.

Introduction and related works

Adversarial attacks and defences: Though machine learning algorithms perform well under normal conditions, they can fail with cleverly crafted inputs called adversarial samples, raising security concerns in many applications. White-box attacks are attacks wherein the attacker can access model predictions, parameters and training data. Popular attacks in this setting are BIM(Kurakin, Goodfellow, and Bengio (2016)), MIM(Dong et al. (2018)), FGSM(Goodfellow, Shlens, and Szegedy (2015)) and Projected Gradient Descent (henceforth abbreviated as PGD)(Madry et al. (2017)) among which PGD attacks are considered one of the strongest white-box attacks in practice. Prior works have proposed various defence techniques against adversarial attacks, among which the seminal work of Madry et al. (2017)

Copyright © 2025, Association for the Advancement of Artificial Intelligence (www.aaai.org). All rights reserved.

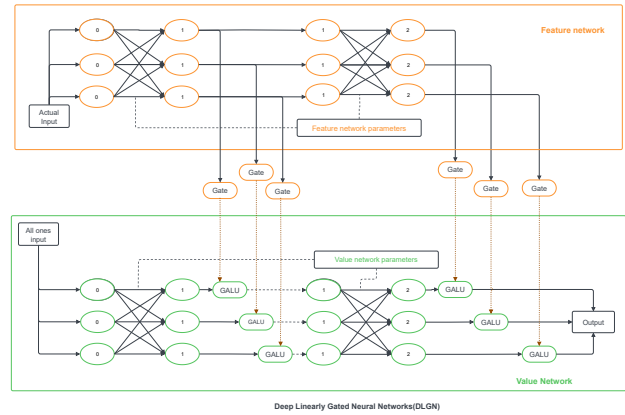


Figure 1: Deep Linearly Gated Networks (DLGN) network architecture. $GALU = x * Gate(x)$

stands out as one of the principled methods. They view defending adversarial attacks as solving a min-max optimization problem wherein the inner maximization aims to get the best possible adversarial samples at a given model state. They solve the inner maximization by using the PGD attack and call it *adversarial training* (Appendix Algorithm 1) (abbreviated as PGD-AT henceforth).

Interpretation of robustness: The arms race between adversarial attacks and defences has also led to many works which instead analyse the adversarial attacks in several ways like distribution shift analysis (Gavrikov and Keuper (2022)), feature representation analysis by ideas like inversion (Boychev (2023), Engstrom et al. (2019)), Fourier spectrum analysis (Lin, Gao, and Sang (2022), Sharma, Ding, and Brubaker (2019), Yin et al. (2019), Wang et al. (2020), Rahaman et al. (2019)), principal component analysis (Gavrikov and Keuper (2022)), shapely value analysis (Chen, Ren, and Yan (2022)).

In this work, we consider a recently proposed novel neural network architecture that is much more amenable to adversarial training analysis.

Deep Linearly Gated Networks: Relu activation can be viewed as the product of input and gates that are off/on. These gates trigger certain pathways in the network to be active/inactive. Lakshminarayanan and Vikram Singh (2020)

propose a unique approach by viewing model training as active sub-network learning in Relu-activated neural networks. Neural networks can be viewed as model input being mapped into the path space (path space representation given by neural path features (NPF)) and combined (coefficients of these combinations are given by neural path values (NPV)) in the path space to generate model output logits (Refer Equation (9) for more details). They introduce Deep Gated Neural Network (DGN) architecture to demonstrate the role of active sub-network learning that has two nearly identical sub-networks: *feature network*, which is responsible for extracting features and providing gating signals (thereby solely encoding NPFs); *value network*, which aggregates the features extracted by the feature network (thereby solely encoding NPVs) to produce the final model prediction.

Model with enhanced interpretability: A follow-up study by Lakshminarayanan, Singh, and Rajkumar (2022) show that interpreting the value network *visually* is meaningless in DGN networks. However, interpreting feature network is still hard due to the non-linearity in the feature network layers. So, to improve the interpretability of DGNs, they propose a new architecture, namely *Deep Linearly Gated Neural Networks (DLGN)* (see Figure 1 for network architecture) wherein the gating signals are completely moved out of the feature network, rendering the transformations in the feature network entirely linear. The DLGN architecture offers significant interpretability advantages compared to standard architectures due to the linear feature network.

Goal: We use the enhanced interpretation capabilities of the DLGN model to compare and contrast standard training (henceforth abbreviated as STD-TR) and adversarial training by analysing the model’s internals. We use ideas like hyperplane analysis, which are unique to DLGN architecture, unlike standard architectures, and ideas from feature visualization and path-view in neural networks to give multi-dimensional insights into robustness.

Our Contributions

- We merge layers in the feature network of DLGN architectures to obtain a single effective linear transformation per layer, which is unique to our work. This reveals novel insights into hyperplanes and their resemblance to principal components in PGD-AT and STD-TR models. Our analyses show that hyperplanes in PGD-AT (FC) models are farther from data points compared to STD-TR (FC) models and play a key role in enhancing robustness.
- We analyze path activity among classes by examining the active-subnetwork overlap (employing neural path kernel) in PGD-AT and STD-TR FC models. Our findings indicate that PGD-AT models generate more diverse active subnetworks and can avoid active subnetwork overlaps with different classes during an attack.
- We quantitatively compare active gate overlaps among classes using the intersection-over-union idea. This reveals that adversarially trained models can prevent significant gating pattern changes and avoid overlap of attack-induced gating changes with those of other classes.

- Using visualization ideas, we interpret the representations used by PGD-AT and STD-TR models in the feature network of DLGN.

Analysis of hyperplanes in feature network of fully connected robust and standard models

Notations Let θ_f and θ_v be parameters of the model with L layers in feature network and value network respectively and more specifically with $W_l \in R^{m_{l-1}, m_l}$ being the weight at layer l of feature network, $b_l \in R^{m_l}$ being the bias at layer l of the feature network. Let $x_l \in R^{m_l}$ be the feature network output at layer l , p be one of the paths among total P paths passing from each input node to each output node, $G_{x, \theta_f}^{l,p}$ be the gate for input x at the node contained in path p at layer l and x_p be the input node at node contained in path p . Then, from work [Lakshminarayanan and Vikram Singh (2020)], the gate information is encoded in the neural path features (NPF) $\Phi_{x, \theta_f} \in R^P$ (Equation (1b)) as the product of input and gates along a path. Similarly, the weight information is encoded in the neural path value (NPV) $\vartheta_{\theta_v} \in R^P$ (Equation (1c)) as the product of weights along a path. The final model output logit per output node is given by $\hat{y}(x)$, which can be expressed as per Equation (1d). Refer Appendix Figure 9 for more details.

$$G_{x, \theta_f}^l = \sigma(\beta * (W_l^T x_{l-1} + b_l)) \in R \quad (1a)$$

$$\Phi_{x, \theta_f} = \{x_p \prod_{l=1}^L G_{x, \theta_f}^{l,p}, \quad p \in [P]\} \in R^P \quad (1b)$$

$$\vartheta_{\theta_v} = \{\prod_{l=1}^L \theta_v^{l,p}, \quad p \in [P]\} \in R^P \quad (1c)$$

$$\hat{y}(x) = \langle \Phi_{x, \theta_f}, \vartheta_{\theta_v} \rangle \in R \quad (1d)$$

where σ is the sigmoid activation i.e $\sigma(x) = \frac{1}{1 + e^{-x}}$

Consider a DLGN architecture with fully connected layers where the feature network is entirely linear. At each *feature network layer* l , the effective linear transformation can be obtained by merging all preceding layers up to l , with effective weights $E_l \in R^{m_0, m_l}$ and bias $p_l \in R^{m_l}$. **Note that this analysis is not possible in standard neural networks due to the non-linearity between layers.** The output at layer l would produce m_l gates and each gate’s effective weight $\in R^{m_0}$ would be a hyperplane acting on input in m_0 -dimensional space. A gate is active/inactive based on which side of the hyperplane the input x lies.

$$\begin{aligned} \hat{y}(x + \delta) &= \sum_{p=1}^P \Phi_{x+\delta, \theta_f} * \vartheta_{\theta_v} \\ &= \sum_{p=1}^P [(x^p + \delta^p) \prod_{l=1}^L \sigma\{E_l^p(x + \delta) + p_l\}] * \vartheta_{\theta_v} \end{aligned} \quad (2a)$$

From Equation (2a) for a perturbation δ in input x , larger values of $E_l^p x + p_l$ reduce the gate’s sensitivity in path p , thereby enhancing adversarial robustness. Informally, if a point is farther from a hyperplane, it requires either larger dimension-wise perturbations or small perturbations across many dimensions to flip the gate¹.

¹In experiments, β is set high to approximate a step function

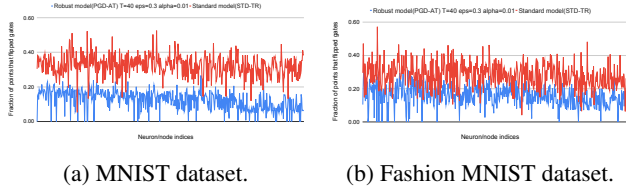


Figure 2: PGD-AT vs STD-TR FC-DLGN -W128-D4 flip distribution. The Y-axis denotes the fraction of points that flipped the gate at node indices on the X-axis.

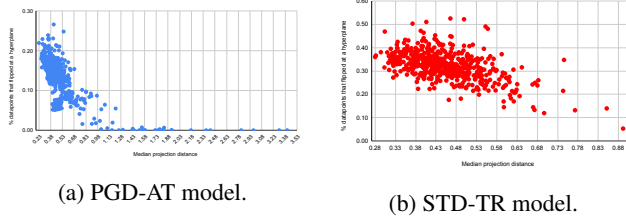


Figure 3: Flip distribution per hyperplane(y-axis) vs. median projection distance(x-axis) in MNIST dataset. Each point indicates a hyperplane.

Hyperplane analysis in real-world dataset

We trained a DLGN with four fully connected layers (width 128) on the MNIST and Fashion MNIST datasets using both standard training and adversarial training (PGD-AT, $\epsilon = 0.3, \alpha = 0.1, T = 40$). Adversarial attacks used PGD with 40 steps and $\epsilon = 0.3$. When an adversarial example crosses to the opposite side of the hyperplane compared to the original input, the gate is considered flipped (from active to inactive or vice versa). As shown in Figure 2, fewer data points flipped at each hyperplane in PGD-AT models than in STD-TR models. We inspect the projection distance of points from each hyperplane of fully connected layers in the feature network of DLGN given by the expression $\frac{E_l^T x + p_l}{\|E_l\|_2}$. Guided by the mathematical intuition at Equation (2a), we experimentally (in Figures 3a and 3b) show that larger median projection distances results in less gate flipping thereby enhancing robustness. We plot the median projection distance over all samples from each hyperplane across all layers (see Figure 4 and Appendix Figure 10) and found that the median distance from hyperplane is relatively higher in PGD-AT models than STD-TR models at many hyperplane indices. This trend is also reflected in projection distance histograms, which show significant differences between standard and robust models (see Appendix Figure 12). In Figure 5, we compare masking gates with the highest median projection distance, masking gates with the lowest median projection distance and masking gates randomly in PGD-AT and STD-TR models. Results show that median-based masking significantly reduces PGD-40 and clean accuracies in PGD-AT models, highlighting the importance of gates with higher median distances for robustness.

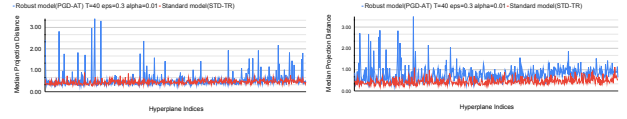


Figure 4: PGD-AT vs STD-TR FC-DLGN -W128-D4 median projection distance. The left image is on MNIST, and the right image is on the Fashion MNIST dataset. The Y-axis denotes the median projection distance of data points at node/hyperplane indices on the X-axis.

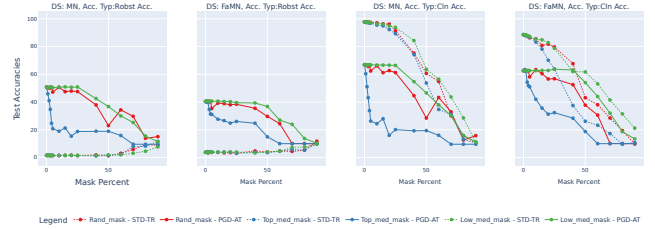


Figure 5: Robust and clean accuracies of PGD-AT and STD-TR FC-DLGN _W128_D4 models with random gate masking vs. masking gates with the highest median projection distance vs masking gates with lowest median projection distance. Dotted lines are for STD-TR models and solid lines are for PGD-AT models.

Hyperplane analysis in synthetic XOR dataset

We constructed a 2D XOR dataset (see Appendix Figure 13) with a gap λ from the axes, ensuring that points satisfy $|x| > \lambda$ and $|y| > \lambda$. This design allows setting $\epsilon \leq \lambda$ during adversarial training, where ϵ represents the perturbation boundary without changing the ground truth labels. Using a DLGN with 3 fully connected layers (width 4), we trained models via both standard (STD-TR) and adversarial training (PGD-AT, $\epsilon = 0.3, T = 40$). The decision boundaries of PGD-AT models are closer to optimal compared to STD-TR (see Appendix Figures 14a and 14b), ensuring that adversarial examples within L_∞ bounds ($\epsilon = 0.3$) are correctly classified only by PGD-AT. Visualization of hyperplanes at each layer of the feature network (see Figure 6) shows that PGD-AT models learn hyperplanes positioned farther from the data points than STD-TR models. This trend increases in deeper layers as compared to earlier ones. So, we conclude that hyperplanes with larger projection distances from data points are key in enhancing robustness.

PCA analysis in robust and standard models

Principal Component Analysis (PCA) minimizes point-to-hyperplane distances, while we saw that the PGD-AT process increases these distances to improve robustness. This fundamental difference motivates us to investigate the impact of PCA on adversarial training. We *embedded* PCA projection operation into the input layer of a DLGN architecture, ensuring both training and inference accounted for the transformation. This also ensures that the adversary has knowledge of the operation and doesn't change the dimensions of the model input. To offset the reduced capacity from

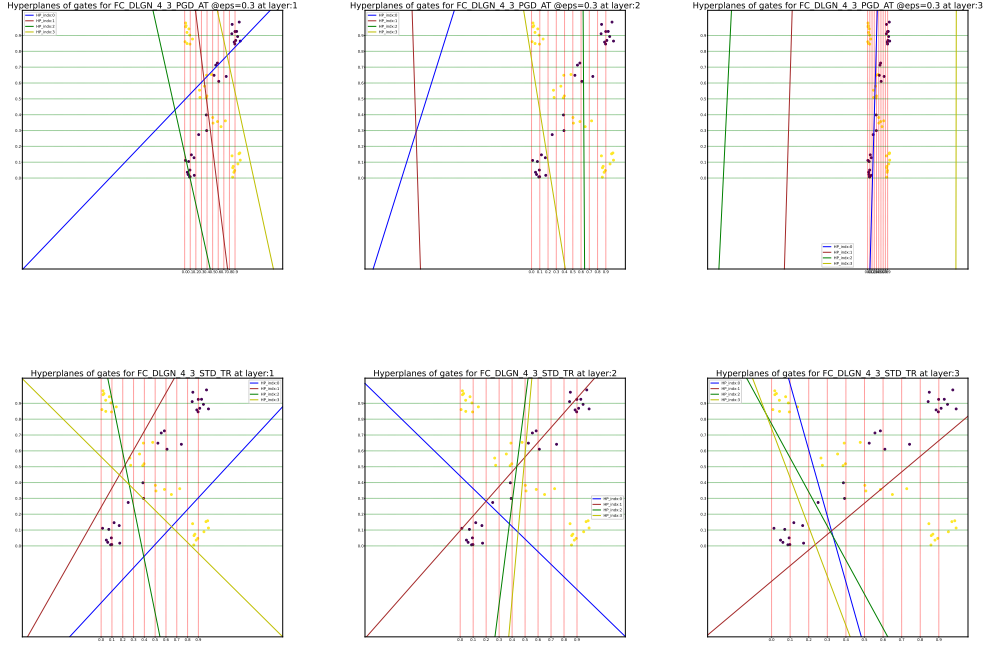


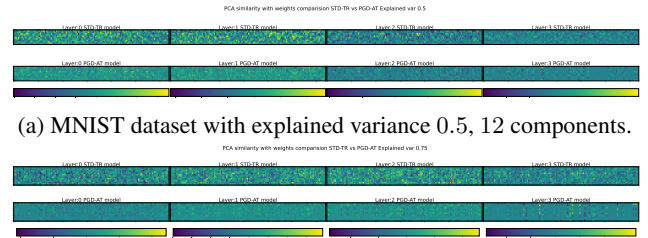
Figure 6: Hyperplane plots of PGD-AT vs STD-TR models in FC-DLGN -W4-D3. Row 1 indicates the PGD-AT model, and row 2 indicates the STD-TR model. Columns 1-3 indicate layers 1-3. Each image contains four hyperplanes since the width at each layer is 4.



Figure 7: DLGN model trained with PCA embedded layer at different levels of dimensionality reduction on MNIST and Fashion MNIST datasets.

PCA’s dimensionality reduction, we increased the model’s width at all layers to keep the capacity constant across all models under comparison. Experiments on MNIST and Fashion MNIST (see Figure 7) reveal a significant drop in both PGD-40 and clean accuracy in PGD-AT models compared to STD-TR models, indicating that PCA negatively affects adversarial robustness. This suggests that PCA’s dimensionality reduction conflicts with the robustness objectives of adversarial training.

To further investigate the relation of principal components with hyperplanes in PGD-AT models, we computed the top k principal components $P \in \mathbb{R}^{m_0 \times k}$ of the MNIST and Fashion MNIST training datasets and analyzed their similarity with the effective weights $E_l \in \mathbb{R}^{m_0 \times m_l}$ of the feature network layers in models, given by $C_l = P^T E_l \in$



(a) MNIST dataset with explained variance 0.5, 12 components.
 (b) Fashion MNIST dataset with explained variance 0.75, 15 components.

Figure 8: Effective weights with top PCA components in PGD-AT (bottom row) and STD-TR (top row) using FC-DLGN -W128-D4 architecture.

$\mathbb{R}^{k \times m_l}$. Results show higher alignment between principal components and hyperplanes in STD-TR models compared to PGD-AT models (see Figure 8 and Appendix Figures 15 and 16). This supports the observation that PGD-AT hyperplanes are positioned to maximize robustness rather than minimize point-to-hyperplane distance, leading to lower similarity with principal components.

Dataset	Train Type	$\log_2 \Psi_{orig}^D$	$\log_2 \Psi_{orig}^S$	$\log_2 \Psi_{adv}^D$	$\log_2 \Psi_{adv}^S$	$\log_2 \Psi_{a,o}^D$	$\log_2 \Psi_{a,o}^S$
MNIST 3vs8	PGD-AT STD-TR	24.8	26.9	25	26.4	24.8	26.1
		24.6	27.3	27.1	28	26.9	26.2
MNIST 1vs7	PGD-AT STD-TR	22.8	27.3	25	26.9	23.9	26.3
		20	27	27.3	28	25.8	26.2
MNIST 0vs6	PGD-AT STD-TR	22.9	27.1	24.7	26.4	24	26.3
		21.2	27.6	27.8	28.4	26.5	26.3
MNIST 1vs5	PGD-AT STD-TR	22.9	26.9	25	26.4	24.1	26.1
		20.42	27.5	21	28.4	27.2	20.7
MNIST 3vs9	PGD-AT STD-TR	24.4	26.8	24.6	26.2	24.4	26
		23.7	27.4	26	28.3	27	25
MNIST 2vs9	PGD-AT STD-TR	24	27.1	24.6	26.7	24.2	26.5
		23.3	27.3	23.5	28.5	27	23.5

Table 1: FC-DLGN -W128-D4 architecture PGD-AT vs STD-TR model subnetwork overlap metrics over original and adversarial examples. The task is binary classification over the MNIST dataset in column 1, and the model has a single output node for classification. PGD-AT rows are highlighted in bold for better readability.

Active subnetwork overlap in fully connected robust vs standard models

Adversaries can alter the output only by changing the active pathways (i.e., NPF). Due to this significance, we measure the overlap in active pathways among samples of the same class and between different classes. The Neural Path Kernel (NPK) Ψ (as per Equation (3a)) is the gram-matrix of NPFs that measures the overlap of active pathways between pairs of examples. We consider a binary classification task and define two metrics to measure overall NPK overlap between different classes Ψ^D and between the same classes Ψ^S as defined in Equations (3b) and (3c).

$$\Psi_{\theta}(s, s') = \langle \Phi_{x_s, \theta}, \Phi_{x_{s'}, \theta} \rangle \quad s, s' \in [n] \in R^{n, n} \quad (3a)$$

where θ is parameters of the model, $\Phi_{x, \theta} \in R^P$ is the NPF

$$\Psi^S = \sum_{i, j} \Psi_{\theta}(i, j) \quad \forall i, j : y_{true}^i = y_{true}^j \quad (3b)$$

$$\Psi^D = \sum_{i, j} \Psi_{\theta}(i, j) \quad \forall i, j : y_{true}^i \neq y_{true}^j \quad (3c)$$

We obtain these two metrics among adversarial (Ψ_{adv}), original samples (Ψ_{orig}) and between adversarial and original samples ($\Psi_{adv, org}$) for models trained using PGD-AT and STD-TR on two class datasets (see Table 1 for MNIST

dataset and Appendix Table 5 for Fashion MNIST dataset). Firstly, $\Psi_{orig}^D < \Psi_{adv}^D$ & $\Psi_{orig}^D < \Psi_{adv, org}^D$ for both PGD-AT and STD-TR models. This indicates that adversarial attacks increase active subnetwork overlap between different classes as compared to original samples in an attempt to change the model prediction. Secondly, $\Psi_{adv, org}^D$ for PGD-AT is always lesser than $\Psi_{adv, org}^D$ for STD-TR models. Also Ψ_{adv}^D for PGD-AT is lesser than Ψ_{adv}^D for STD-TR models in most cases. These indicate that the active pathways triggered by adversarial examples overlap less with original examples or adversarial examples of another class in the PGD-AT model. Thirdly, Ψ_{adv}^S & Ψ_{orig}^S for PGD-AT is always lesser than that in STD-TR. So, the trends so far indicate that the PGD-AT training process learns to map the input to a more diverse path space where overlap among the same class is lesser, and PGD-AT models control subnetwork overlap between different classes during an attack compared to STD-TR models.

Analysis and interpretation of gating patterns in robust vs standard models in convolutional architectures

Notations *The following are the notations in convolutional architectures:* Let $X \in R^{N, 1, W, H}$ be the whole training dataset with the size of each sample being $1 \times W \times H$. Let $X_c \in R^{N_c, 1, W, H}$ be the training dataset per class with N_c being the number of samples of class c . Let L be the number of layers, C_l be the number of output channels in layer l of feature network (in our experiments for simplicity, we keep C_l same across all layers) and W, H be the width, height of output at all feature network layers (since we fix padding=1, kernel size=3, width and height of the output stays same across all layers). Let the output at each feature network layer per class be $F_l \in R^{N_c, C_l, W, H}$. For original examples, let the output combined across all feature network layers be $F^{orig} \in R^{L, N_c, C_l, W, H}$ and for adversarial examples let it be $F^{adv} \in R^{L, N_c, C_l, W, H}$. "mode" is either adversarial or original examples throughout the paper.

Analysis of gating patterns in robust and standard models

The gates generated in the feature network are the only input representations accessible to the model's value network; hence, their study sheds light on robust models' behaviour. Our goal is to measure the extent of active gate overlap among different class-pairs in *convolutional* DLGN architectures quantitatively using the idea of intersection-over-union (IOU) and qualitatively by visually inspecting the difference in active gate counts with and without attacks (refer Appendix Tables 6 and 7). The number of active gates per class at each pixel in F_l across all L layers is given by Equa-

Src Class	Train Type	Quantity	Class 0	Class 1	Class 2	Class 3	Class 4
0	PGD-AT	IOU_{agc}^{adv}	100	70.2	83	82.7	81.8
		IOU_{agc}^{org}	100	66.2	79.3	79.4	77.9
	STD-TR	IOU_{agc}^{adv}	100	78.1	84.7	82	81
		IOU_{agc}^{org}	100	59.7	74.7	75	73.1
1	PGD-AT	IOU_{agc}^{adv}	70.2	100	74.9	75.8	74.7
		IOU_{agc}^{org}	66.2	100	71.9	74.3	71.9
	STD-TR	IOU_{agc}^{adv}	78.1	100	82.7	79.5	80
		IOU_{agc}^{org}	59.7	100	63.7	66.5	65.6
2	PGD-AT	IOU_{agc}^{adv}	83	74.9	100	86.9	84.3
		IOU_{agc}^{org}	79.3	71.9	100	84.7	80.5
	STD-TR	IOU_{agc}^{adv}	84.7	82.7	100	82.4	83.9
		IOU_{agc}^{org}	74.7	63.7	100	80.7	74.2
3	PGD-AT	IOU_{agc}^{adv}	82.8	75.8	86.9	100	82.7
		IOU_{agc}^{org}	79.4	74.3	84.7	100	78.6
	STD-TR	IOU_{agc}^{adv}	82	79.5	82.4	100	77.5
		IOU_{agc}^{org}	75	66.5	80.7	100	73.4
4	PGD-AT	IOU_{agc}^{adv}	81.8	74.7	84.3	82.7	100
		IOU_{agc}^{org}	77.9	71.9	80.5	78.6	100
	STD-TR	IOU_{agc}^{adv}	81	80.2	83.9	77.8	100
		IOU_{agc}^{org}	73.1	65.6	74.2	73.4	100

Table 2: CONV DLGN -N128-D4 PGD-AT vs STD-TR model IOU of active gate count between class-pairs over adversarial and original examples in MNIST dataset. Only the first four classes are reported here and rest are in Appendix Table 9

tion (11b).

$$Gate(x) = \begin{cases} 1, & \text{if } x > 0 \\ 0, & \text{otherwise} \end{cases} \quad (4a)$$

$$\Lambda_c^{mode} = \sum_{i=1}^{N_c} Gate(F^{mode}(X_c)), \in R^{L, C_i, W, H} \quad (4b)$$

The procedure to obtain the IOU of active gate count of class c_1 and c_2 ($IOU_{agc}(c_1, c_2)$) is illustrated in the Appendix.

We trained a DLGN with 4 convolutional layers, each having 128 filters (padding 1, stride 1, kernel size 3), followed by an adaptive average pooling layer and a fully connected classification layer. Adversarial training (PGD-AT) was performed on the MNIST dataset with $\epsilon = 0.3, T = 40, \alpha = 0.005$, and we measured the Intersection-over-Union (IOU) of active gate overlaps between different class pairs over original (IOU_{agc}^{org}) and adversarial (IOU_{agc}^{adv}) samples (see Table 2 for MNIST and Appendix Table 8 for Fashion MNIST). First, IOU_{agc}^{org} for PGD-AT models is consistently higher than for STD-TR models, indicating that gate overlap among classes is initially larger in PGD-AT models. Second, for both PGD-AT and STD-TR, adversarial attacks increase the gate overlap, as $IOU_{agc}^{adv} > IOU_{agc}^{org}$ across all class pairs. Third, the increase in gate overlap ($IOU_{agc}^{adv} - IOU_{agc}^{org}$) is larger in STD-TR models com-

pared to PGD-AT models, demonstrating that minimizing gate overlap among different classes during adversarial attacks is a key feature of PGD-AT models.

Interpretation of gating patterns in robust vs standard models

We aim to further analyze gating patterns by identifying the images that most effectively trigger them. We begin by inverting gating signals in the DLGN model trained in both PGD-AT and STD-TR modes. Then, we explore more complex gating patterns through inversion. We start by asking: *What is the input image that best simulates the dominant gating signals of an entire class?* The procedure to obtain such an input image I for class c is as follows:

1. Obtain the active gate count per pixel Λ_c^{mode} as per Equation (11b). Also obtain the inactive gate count per pixel $\eta_c^{mode} : \eta_c^{mode}(i) = N_c - \Lambda_c^{mode}(i)$.
2. Obtain the dominating gate active-inactive trend per pixel $\rho_{c,\lambda}^{mode}$ as per Equation (5). Here λ is the threshold which indicates the percentage of gates that has to be active(inactive) among all the class samples to be considered as active(inactive) overall.

$$\rho_{c,\lambda}^{mode}(i) = \begin{cases} 1, & \text{if } \Lambda_c^{mode}(i) > \lambda * N_c \\ -1, & \text{if } \eta_c^{mode}(i) > \lambda * N_c \end{cases} \quad (5)$$

3. Let I be the input image under optimization, F^{mode} be the feature maps at the feature network for input I as usual as per our notations. Then, we define a loss function $L(I, \rho^{mode})$ as per Equation (6). This loss function objective is to obtain I such that its feature maps sign at each pixel matches with the dominating gate pattern.

$$L(I, \rho^{mode}) = \sum_i \log(1 + e^{-\rho(i) * \tanh(F(i))}) \quad (6)$$

4. Now we need to optimize I over the loss function. We explored gaussian blur on gradient and I route but found the results to be satisfactory. However we found the optimization mentioned in Equation (7) provides good results.

$$I_t = I_{t-1} + \alpha \text{sign}(\nabla_{I_t} L) \quad (7)$$

5. Start with $I_0 = 0$ and perform optimization as per Equation (7) on the loss function Equation (6) for T steps. That is, repeat step 3,4 T times.

We set $\alpha = 0.1, T = 50$, and $\lambda = 0.9$ in our experiments. The visualizations for DLGN -N128-D4 trained on the MNIST, Fashion MNIST dataset are presented in Table 3. Dominant gating patterns from original examples capture critical class information, with images inverting these patterns (I^{org}) clearly resembling their respective classes. The PGD-AT model produces sharper, more distinct class features than the STD-TR model, indicating better utilization of model capacity by PGD-AT. In the STD-TR model, for example, I_5^{org} can be made to resemble I_8^{org} with less changes, indicating that one can change input image that triggers dominant gates of class 5 to the image that triggers


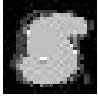

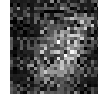

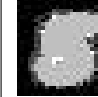





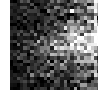



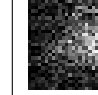
Class (c)	PGD-AT I^{org}	PGD-AT I^{adv}	STD-TR I^{org}	STD-TR I^{adv}	PGD-AT I^{ado}	PGD-AT I^{amo}	STD-TR I^{ado}	STD-TR I^{amo}
MNIST 5								
FMNIST Sneaker								

Table 3: Image I which triggers dominating gating pattern per class over CONV DLGN -N128-D4 model obtained on adversarial examples (columns 3,5), obtained on original examples (columns 2,4), obtained on adversarial examples alone but not on original examples (columns 6,8) and obtained both on original examples and adversarial examples (columns 7,9). Visualization loss function is as per Equation (6), $\lambda = 0.9$, $\alpha = 0.1$, optimization is as per Equation (7). We have reported a few classes for brevity. Detailed results are in Appendix Tables 10 and 11

dominant gates of class 8 easily, thereby showing the brittle nature of representations used by STD-TR models. Furthermore, in PGD-AT, I^{adv} retain class resemblance, while STD-TR's I^{adv} images are noisy. This indicates PGD-AT prevents adversaries from activating semantically unrelated gating patterns, maintaining class information with slight degradation. Next, we aim to find the input images (I^{ado}) that best simulate gating signals dominantly active during adversarial attacks but not in original examples for an entire class and the images (I^{amo}) that simulate gate patterns active in both adversarial and original examples for an entire class. The visualization process remains the same, except for changes in the computation of ρ . I_c^{ado} is derived using ρ_c^{ado} (see Equation (8a)), while I_c^{amo} uses ρ_c^{amo} (see Equation (8b)).

$$\rho_{c,\lambda}^{ado}(i) = Gate\{\rho_{c,\lambda}^{adv}(i) - Gate(\rho_{c,\lambda}^{org}(i))\} \quad (8a)$$

$$\rho_{c,\lambda}^{amo}(i) = \rho_{c,\lambda}^{adv}(i) * Gate(\rho_{c,\lambda}^{org}(i)) \quad (8b)$$

We report visualized images I_c^{ado} , I_c^{amo} for both DLGN PGD-AT and STD-TR models as before trained on MNIST, Fashion MNIST dataset in Table 3. In the PGD-AT model, I_c^{ado} does not produce meaningful inputs, as these patterns are framed images with no resemblance to any class, even using the same visualization method and parameters. This contrasts with I_c^{adv} , where adversarial examples resemble class images, indicating that only the dominant active gating patterns from original examples are meaningful in PGD-AT models. In the STD-TR model, both I_c^{adv} and I_c^{ado} appear similar, with I_c^{amo} showing little resemblance to class images, highlighting significant differences between active gates triggered by adversarial and original examples. In PGD-AT, I_c^{amo} shows that adversarial examples trigger a subset of original class gating patterns, maintaining some class resemblance.

Conclusion and future directions

In this work we utilized DLGN architectures to thoroughly study the difference in properties exhibited by PGD-AT and STD-TR models. We analyzed fully connected networks, focusing on properties such as hyperplane alignment, path-

activity and found that PGD-AT models exhibit larger datapoint separation distances from hyperplanes, active pathways triggered during adversarial attacks in PGD-AT models show less overlap with original examples of other classes and less overlap among original samples of same class suggesting better capacity utilization. We examined convolutional networks to show that PGD-AT models reduce gating overlap among different classes during adversarial attacks. Additionally, we used visualization techniques to understand the dominant gating patterns triggered per class in various scenarios for both STD-TR and PGD-AT models shedding light on the nature of representations used by these models. We believe that leveraging the results of our analysis to develop novel algorithms that account for the properties examined could effectively enhance robustness. Extending this analysis to larger and more complex models, such as transformers or other deep architectures, could provide further insights into the generalizability of our findings. While this work focused on PGD-AT, other adversarial training methods could be explored to generalize the understanding of robustness.

References

- Boychev, D. 2023. Interpretable Computer Vision Models through Adversarial Training: Unveiling the Robustness-Interpretability Connection. arXiv:2307.02500.
- Chen, Y.; Ren, Q.; and Yan, J. 2022. Rethinking and Improving Robustness of Convolutional Neural Networks: a Shapley Value-based Approach in Frequency Domain. In Koyejo, S.; Mohamed, S.; Agarwal, A.; Belgrave, D.; Cho, K.; and Oh, A., eds., *Advances in Neural Information Processing Systems*, volume 35, 324–337. Curran Associates, Inc.
- Dong, Y.; Liao, F.; Pang, T.; Su, H.; Zhu, J.; Hu, X.; and Li, J. 2018. Boosting Adversarial Attacks with Momentum. In *2018 IEEE/CVF Conference on Computer Vision and Pattern Recognition*, 9185–9193.
- Engstrom, L.; Ilyas, A.; Santurkar, S.; Tsipras, D.; Tran, B.;

and Madry, A. 2019. Adversarial Robustness as a Prior for Learned Representations. arXiv:1906.00945.

Gavrikov, P.; and Keuper, J. 2022. Adversarial Robustness through the Lens of Convolutional Filters. In *2022 IEEE/CVF Conference on Computer Vision and Pattern Recognition Workshops (CVPRW)*. IEEE.

Goodfellow, I. J.; Shlens, J.; and Szegedy, C. 2015. Explaining and Harnessing Adversarial Examples. arXiv:1412.6572.

Kurakin, A.; Goodfellow, I.; and Bengio, S. 2016. Adversarial examples in the physical world. arXiv:1607.02533.

Lakshminarayanan, C.; Singh, A. V.; and Rajkumar, A. 2022. Explicitising The Implicit Interpretability of Deep Neural Networks Via Duality. arXiv:2203.16455.

Lakshminarayanan, C.; and Vikram Singh, A. 2020. Neural Path Features and Neural Path Kernel : Understanding the role of gates in deep learning. In Larochelle, H.; Ranzato, M.; Hadsell, R.; Balcan, M.; and Lin, H., eds., *Advances in Neural Information Processing Systems*, volume 33, 5227–5237. Curran Associates, Inc.

Lin, Z.; Gao, Y.; and Sang, J. 2022. Investigating and Explaining the Frequency Bias in Image Classification. arXiv:2205.03154.

Madry, A.; Makelov, A.; Schmidt, L.; Tsipras, D.; and Vladu, A. 2017. Towards Deep Learning Models Resistant to Adversarial Attacks. arXiv:1706.06083.

Rahaman, N.; Baratin, A.; Arpit, D.; Draxler, F.; Lin, M.; Hamprecht, F. A.; Bengio, Y.; and Courville, A. 2019. On the Spectral Bias of Neural Networks. arXiv:1806.08734.

Sharma, Y.; Ding, G. W.; and Brubaker, M. A. 2019. On the effectiveness of low frequency perturbations. In *Proceedings of the 28th International Joint Conference on Artificial Intelligence, IJCAI'19*, 3389–3396. AAAI Press. ISBN 9780999241141.

Wang, H.; Wu, X.; Huang, Z.; and Xing, E. P. 2020. High-Frequency Component Helps Explain the Generalization of Convolutional Neural Networks. In *2020 IEEE/CVF Conference on Computer Vision and Pattern Recognition (CVPR)*, 8681–8691.

Yin, D.; Lopes, R. G.; Shlens, J.; Cubuk, E. D.; and Gilmer, J. 2019. *A fourier perspective on model robustness in computer vision*. Red Hook, NY, USA: Curran Associates Inc.

Appendix

Path view of learning in neural networks

An input to a neural network (with RELU activations) leads to a certain subnetwork being active. The input can be viewed as being mapped to path space wherein the path space representation is given by the neural path feature (NPFs), and the weight of each path is given by neural path value (NPVs). NPF of a path is given by the product of gates along a path and NPV of a path is given by the product of weights along a path. Appendix Figure 9 illustrates this idea of path-view along with concept of NPF,NPV. The overall

network output can be obtained as dot product of the NPFs and NPVs as demonstrated in Equation (9).

$$\begin{aligned}
 NPF.NPV &= V(1,1)W(1,1)U(1,1)x * G(1,1)G(2,1) \\
 &\quad + V(1,2)W(2,2)U(2,1)x * G(1,2)G(2,2) \\
 &\quad + V(1,1)W(1,2)U(2,1)x * G(1,1)G(2,2) \\
 &\quad + V(1,2)W(2,1)U(1,1)x * G(1,2)G(2,1) \\
 NPF.NPV &= U(1,1)G(2,1)[x * V(1,1)G(1,1)W(1,1) \\
 &\quad + x * V(1,2)G(1,2)W(2,1)] \\
 &\quad + U(2,1)G(2,2)[x * V(1,1)G(1,1)W(1,2) \\
 &\quad + x * V(1,2)G(1,2)W(2,1)] \\
 NPF.NPV &= U(1,1)RELU(2,1) + U(2,1)RELU(2,2) \\
 NPF.NPV &= \hat{y} \tag{9a}
 \end{aligned}$$

Algorithm 1: PGD adversarial training for M epochs, given some radius ϵ , adversarial step size α , T PGD steps and a dataset of size N for a network F_θ

```

for  $j = 1 \dots M$  do
  for  $i = 1 \dots N$  do
    // Perform PGD adversarial attack
     $\delta = U(-\epsilon, \epsilon)$ 
    for  $t = 1 \dots T$  do
       $\delta = \delta + \alpha \cdot \text{sign}(\nabla_\delta L(F_\theta(x_i + \delta), y_i^{true}))$ 
       $\delta = \max(\min(\delta, \epsilon), -\epsilon)$ 
    end for
     $\theta = \theta - \nabla_\theta L(F_\theta(x_i + \delta), y_i)$  // Update model weights
    with some optimizer, e.g. SGD
  end for
end for

```

PGD-40 and clean accuracies over MNIST and Fashion MNIST dataset using various architectures are reported at Appendix Table 4.

More analysis of hyperplanes in feature network of PGD-AT and STD-TR models

The median projection distance at each hyperplane in PGD-AT and STD-TR models of DLGN with width 256 (see Appendix Figure 10) and 64 (see Appendix Figure 11) also clearly shows that median distances increase in robust models.

The projection distance histogram at hyperplanes, which shows significant differences in median projection distance between standard and robust models (see Appendix Figure 12), also shows that the projection distance of datapoints is shifted to larger distances in PGD-AT than STD-TR models.

Hyperplane analysis in synthetic XOR dataset

The synthetic XOR 2D dataset constructed with a gap from $x=0.5$ and $y=0.5$ axis is shown in Appendix Figure 13. The decision boundaries of PGD-AT models (see Appendix Figure 14a) are closer to optimal compared to STD-TR (see Appendix Figure 14b), ensuring that adversarial examples

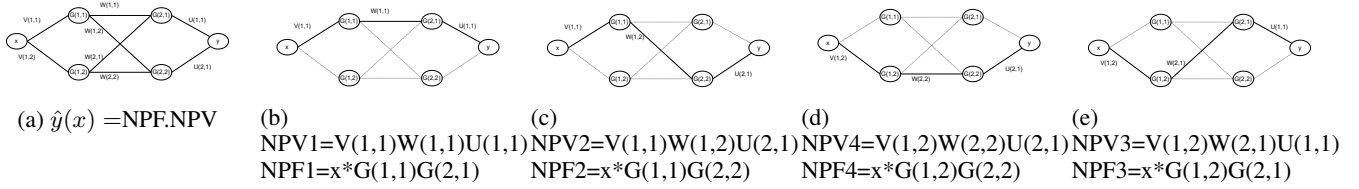


Figure 9: Expressing network output as combination of paths. This gives the path-view of learning in neural networks. Output at a output node is the dot product of NPF and NPV vectors(which are in path space).

Dataset	Architecture	Training Type	PGD-40 Test Acc. ($@\epsilon = 0.3, @\epsilon = 0.2$)	Clean Test Acc.
MNIST	FC-DLGN -W128-D4	PGD-AT	(49.8%, 54.5%)	66.4%
	FC-DLGN -W128-D4	STD-TR	(1.6%, 2.7%)	97.7%
	CONV-DLGN -N128-D4	PGD-AT	(78.9%, 88.9%)	97.5%
	CONV-DLGN -N128-D4	STD-TR	(0.05%, 0.06%)	98.4%
Fashion MNIST	FC-DLGN -W128-D4	PGD-AT	(40.2%, 48.3%)	62.6%
	FC-DLGN -W128-D4	STD-TR	(3.7%, 5.1%)	88.6%
	CONV-DLGN -N128-D4	PGD-AT	(49.8%, 88.9%)	67.8%
	CONV-DLGN -N128-D4	STD-TR	(0%, 0%)	88.9%

Table 4: PGD-AT vs STD-TR model PGD accuracies and clean accuracies

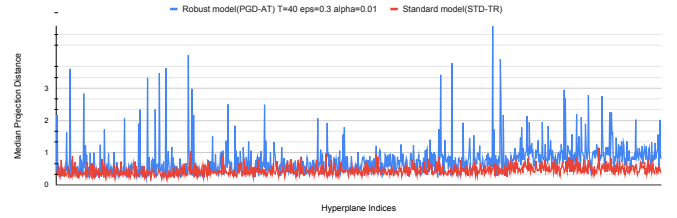
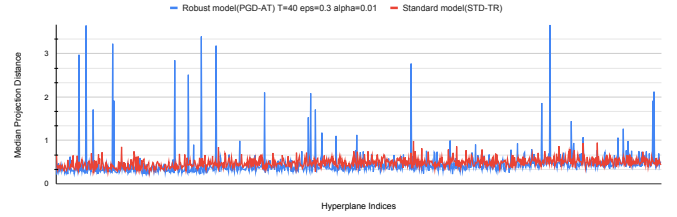


Figure 10: PGD-AT vs STD-TR FC-DLGN -W256-D4 median projection distance. The top image is on MNIST, and the bottom image is on the Fashion MNIST dataset. The Y-axis denotes the median projection distance of data points at node/hyperplane indices on the X-axis.

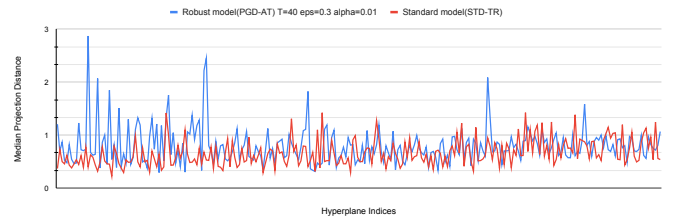
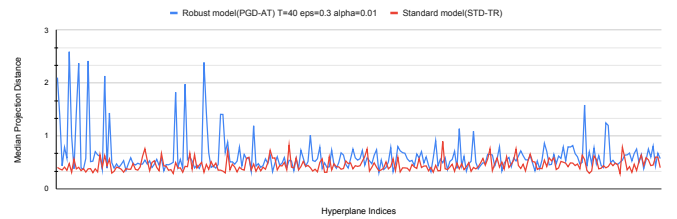


Figure 11: PGD-AT vs STD-TR FC-DLGN -W64-D4 median projection distance. The left image is on MNIST, and the right image is on the Fashion MNIST dataset. The Y-axis denotes the median projection distance of data points at node/hyperplane indices on the X-axis.

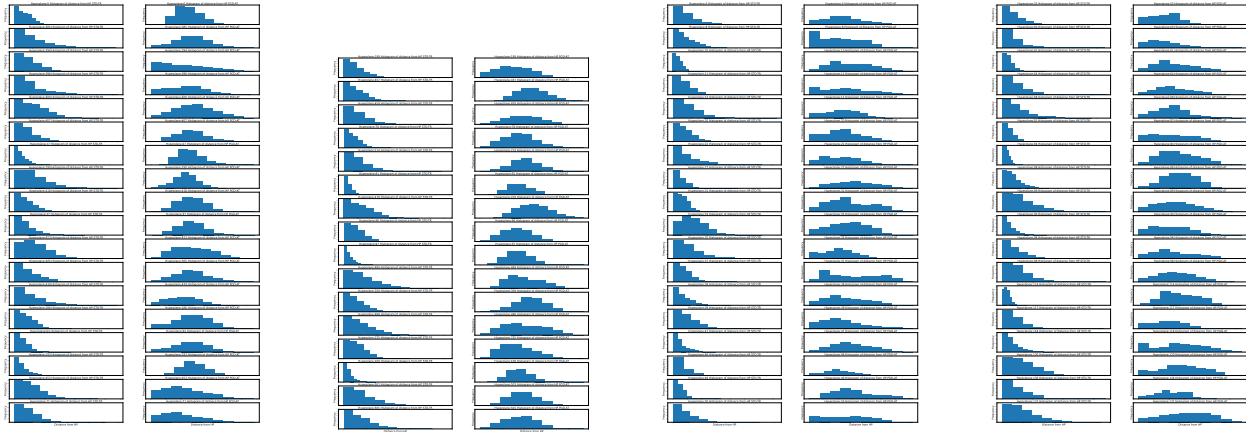


Figure 12: Projection distance distribution at hyperplanes whose medians differ significantly (by 0.5) between standard and robust DLGN models. Each row in each image denotes a hyperplane, with the Y-axis indicating the frequency of occurrence and the X-axis being the distance from that row’s hyperplane. Columns 1,3 are for the STD-TR model, and columns 2,4 are for the PGD-AT model. Both X & Y axis is shared per row. First-row images correspond to the MNIST dataset, and the second-row images correspond to the Fashion MNIST dataset.

within L_∞ bounds ($\epsilon = 0.3$) are correctly classified only by PGD-AT.

PCA ANALYSIS IN ROBUST AND STANDARD MODELS

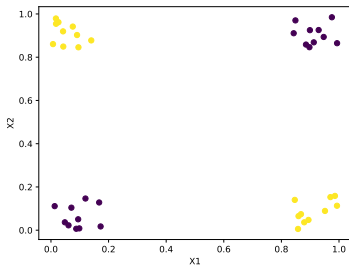
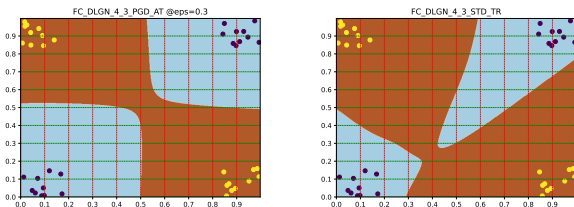


Figure 13: 2D XOR dataset with gap from $x=0.5, y=0.5$ being 0.32 to facilitate PGD-AT with $\epsilon \leq 0.32$.

We report similarity of principal components with hyperplanes of feature network of DLGN with width 256 in Appendix Figure 15 and width 64 in Appendix Figure 16 respectively.



(a) PGD-AT decision boundary. (b) STD-TR decision boundary.

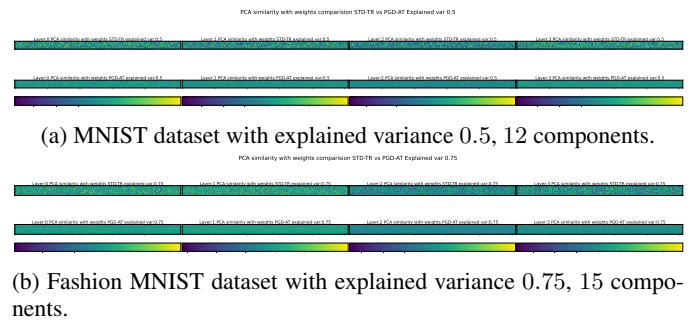
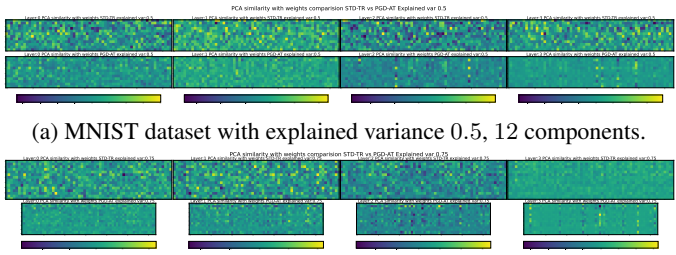


Figure 15: Effective weights with top PCA components in PGD-AT (bottom row) and STD-TR (top row) using FC-DLGN -W256-D4 architecture.



(a) MNIST dataset with explained variance 0.5, 12 components.
 (b) Fashion MNIST dataset with explained variance 0.75, 15 components.

Figure 16: Effective weights with top PCA components in PGD-AT(bottom row) and STD-TR(top row) using FC-DLGN -W64-D4 architecture.

More results in Active subnetwork overlap in PGD-AT vs STD-TR models

The subnetwork overlap metrics for FC-DLGN _W128_D4 architecture trained over the Fashion MNIST dataset is shown in Appendix Table 5.

Qualitative analysis of gating patterns in PGD-AT and STD-TR models

We qualitatively inspect the difference in active gate counts with and without attacks using $\Lambda_c^{adv-diff-org}$ in Equation (10b) that measures the difference in active gate count for adversarial and original examples and is plotted per class for both PGD-AT and STD-TR models as an image of size $L * C_l, W, H$ in Appendix Table 6 and Appendix Table 7.

$$\Lambda_c^{mode} = \sum_{i=1}^{N_c} Gate(F^{mode}(X_c)), \quad \in R^{L, C_l, W, H} \quad (10a)$$

where $mode$ is either original examples or adversarial examples

$$\Lambda_c^{adv-diff-org}(i) = \Lambda_c^{adv}(i) - \Lambda_c^{org}(i), \quad \forall i \in R^{L, C_l, W, H} \quad (10b)$$

Quantitative analysis of gating patterns in PGD-AT and STD-TR models

The number of active gates per class at each pixel in F_l across all L layers is given by Equation (11b).

$$Gate(x) = \begin{cases} 1, & \text{if } x > 0 \\ 0, & \text{otherwise} \end{cases} \quad (11a)$$

$$\Lambda_c^{mode} = \sum_{i=1}^{N_c} Gate(F^{mode}(X_c)), \quad \in R^{L, C_l, W, H} \quad (11b)$$

The following is the procedure to obtain IOU of active gate count of class c_1 and c_2 ($IOU_{agc}(c_1, c_2)$).

1. Compute union of active gate counts at all pixels
 $A_{c_1, c_2}^{mode}(i) = \Lambda_{c_1}^{mode}(i) + \Lambda_{c_2}^{mode}(i) \forall i \in R^{L, C_l, W, H}$

2. Compute intersection of active gate counts at all pixels
 $B_{c_1, c_2}^{mode}(i) = \min(\Lambda_{c_1}^{mode}(i), \Lambda_{c_2}^{mode}(i)) \forall i \in R^{L, C_l, W, H}$
3. Record the indices of U_{c_1, c_2}^{mode} whose value is such that $A_{c_1, c_2}^{mode}(i) > 0.1 * (|X_{c_1}| + |X_{c_2}|)$. Let such an index vector be $\iota_{c_1, c_2} \in R^d$. The intent of this stage is to remove outliers in the union of active gate counts of both classes.
4. Obtain the final intersection as $I_{c_1, c_2}^{mode} = B_{c_1, c_2}[\iota_{c_1, c_2}] \in R^d$. Obtain the final union region as $U_{c_1, c_2}^{mode} = A_{c_1, c_2}[\iota_{c_1, c_2}] \in R^d$
5. Obtain overall average IOU between classes c_1, c_2 as
 $IOU_{agc}^{mode}(c_1, c_2) = \frac{1}{d} \sum_{i=1}^d \frac{I_{c_1, c_2}^{mode}(i)}{U_{c_1, c_2}^{mode}(i)}$

The $IOU_{agc}^{org}, IOU_{agc}^{adv}$ is measured for each pair of classes in Appendix Table 8 for Fashion MNIST dataset.

Interpretation of gating patterns in PGD-AT vs STD-TR models

The visualizations (I^{org}, I^{adv}) for CONV-DLGN _N128_D4 trained on the MNIST, Fashion MNIST dataset are presented in Appendix Table 10. We report visualized images I_c^{adv}, I_c^{org} for both CONV-DLGN _N128_D4 PGD-AT and STD-TR models as before trained on MNIST, Fashion MNIST dataset in Appendix Table 11.

Dataset	Train Type	PGD-40 Acc.	Clean Acc.	$\log_2 \Psi_{orig}^D$	$\log_2 \Psi_{orig}^S$	$\log_2 \Psi_{adv}^D$	$\log_2 \Psi_{adv}^S$	$\log_2 \Psi_{adv,or}^D$	$\log_2 \Psi_{adv,or}^S$
FaMNIST 1vs9	PGD-AT	93.90%	99.70%	22.78	30.45	28.60	31.01	26.43	29.81
	STD-TR	0.00%	100.00%	28.37	31.31	31.25	32.41	31.26	30.01
FaMNIST 3vs8	PGD-AT	76.75%	90.45%	25.92	29.60	28.58	29.29	27.53	28.74
	STD-TR	4.65%	99.30%	25.88	30.39	30.41	31.68	29.04	30.01
FaMNIST 7vs9	PGD-AT	80.75%	87.30%	26.28	29.05	28.29	28.98	27.38	28.54
	STD-TR	0.00%	97.00%	26.58	29.47	31.27	31.67	29.48	29.61
FaMNIST 0vs2	PGD-AT	74.25%	90.10%	26.68	30.04	27.61	29.00	27.06	29.01
	STD-TR	0.00%	97.10%	28.74	30.79	30.10	32.15	30.73	29.17
FaMNIST 4vs5	PGD-AT	92.75%	98.90%	22.70	29.82	29.87	30.24	28.87	29.09
	STD-TR	23.80%	99.00%	27.88	31.16	31.31	31.91	30.55	30.08
FaMNIST 6vs7	PGD-AT	89.00%	98.40%	23.36	29.98	28.47	31.02	31.32	30.30
	STD-TR	23.80%	100.00%	27.35	31.50	23.50	29.21	27.44	28.73

Table 5: FC-DLGN -W128-D4 architecture PGD-AT vs STD-TR model path overlaps metrics over original and adversarial examples. The task is binary classification over the Fashion MNIST dataset in column 2, and the model has a single output node for classification. PGD-AT rows are highlighted in bold for better readability.

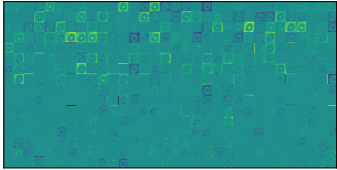
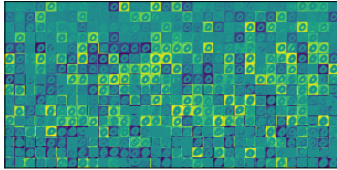
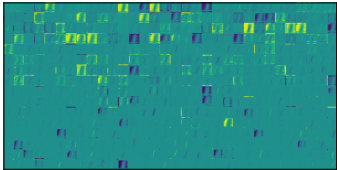
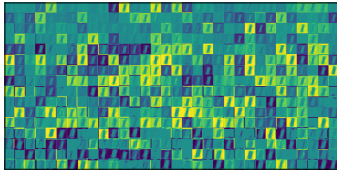
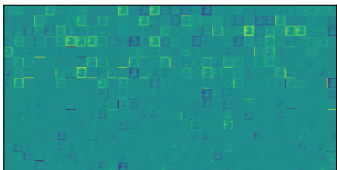
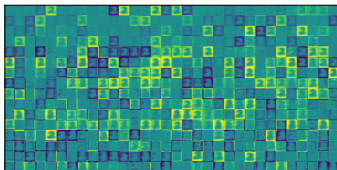
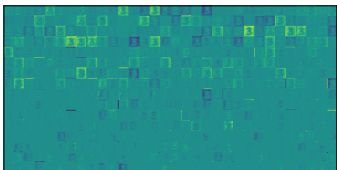
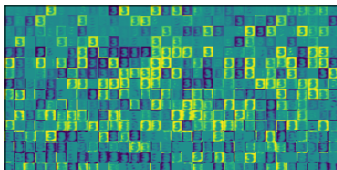
Class (c)	PGD-AT $\Lambda_c^{adv_diff_org}$	STD-TR $\Lambda_c^{adv_diff_org}$
0		
1		
2		
3		

Table 6: $\Lambda_c^{adv_diff_org}$ for PGD-AT and STD-TR models with CONV_N128_D4 DLGN architecture on MNIST dataset. In each cell of the image, every four rows represent a layer's $\Lambda_{l,c}^{adv_diff_org}$

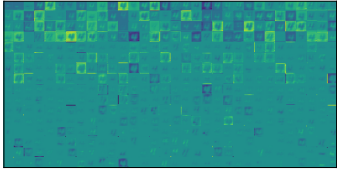
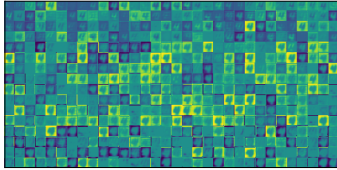
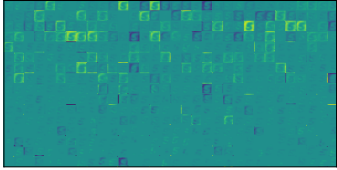
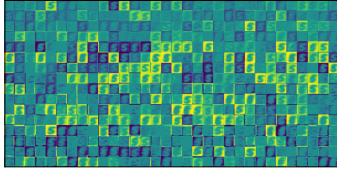
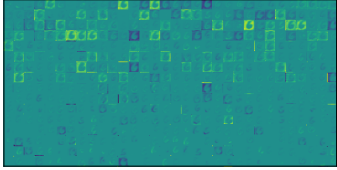
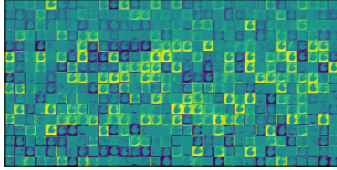
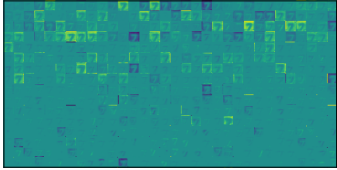
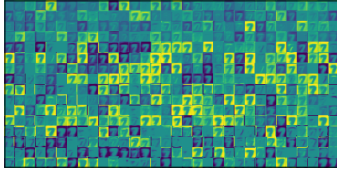
Class (c)	PGD-AT $\Lambda_c^{adv_diff_org}$	STD-TR $\Lambda_c^{adv_diff_org}$
4		
5		
6		
7		

Table 7: $\Lambda_c^{adv_diff_org}$ for PGD-AT and STD-TR models with CONV_N128_D4 DLGN architecture on MNIST dataset. In each cell of the image, every four rows represent a layer's $\Lambda_{l,c}^{adv_diff_org}$

Src Class	Train Type	Quantity	Class 0	Class 1	Class 2	Class 3	Class 4	Class 5	Class 6	Class 7	Class 8	Class 9
0	PGD-AT	IOU_{agc}^{adv}	100.0	81.0	86.9	86.4	86.0	75.0	89.6	73.5	80.9	75.6
		IOU_{agc}^{orig}	100.0	75.6	84.3	83.0	80.9	68.1	86.5	67.4	74.9	69.4
	STD-TR	IOU_{agc}^{adv}	100.0	72.1	78.6	79.4	76.9	67.9	83.2	65.3	73.9	67.7
		IOU_{agc}^{orig}	100.0	57.1	69.2	69.9	65.4	47.3	76.6	44.4	59.6	49.4
1	PGD-AT	IOU_{agc}^{adv}	81.0	100.0	77.8	88.2	80.2	74.2	77.8	74.4	74.0	73.6
		IOU_{agc}^{orig}	75.6	100.0	72.1	85.2	74.5	66.2	71.6	67.5	65.9	66.4
	STD-TR	IOU_{agc}^{adv}	72.1	100.0	68.5	82.4	71.1	64.9	70.9	65.5	66.7	64.2
		IOU_{agc}^{orig}	57.1	100.0	51.0	72.8	55.1	45.9	52.1	44.9	46.8	45.4
2	PGD-AT	IOU_{agc}^{adv}	86.9	77.8	100.0	82.3	91.3	76.0	93.1	73.5	84.8	77.5
		IOU_{agc}^{orig}	84.3	72.1	100.0	77.4	89.8	69.2	91.4	67.2	78.8	72.6
	STD-TR	IOU_{agc}^{adv}	78.6	68.5	100.0	73.1	86.3	67.0	83.7	65.4	76.9	68.8
		IOU_{agc}^{orig}	69.2	51.0	100.0	58.4	81.0	48.5	81.9	45.3	65.2	54.4
3	PGD-AT	IOU_{agc}^{adv}	86.4	88.2	82.3	100.0	84.7	75.0	83.0	74.7	77.7	75.2
		IOU_{agc}^{orig}	83.0	85.2	77.4	100.0	79.7	67.7	78.0	68.3	70.8	68.5
	STD-TR	IOU_{agc}^{adv}	79.4	82.4	73.1	100.0	75.4	68.4	77.5	68.2	71.6	68.3
		IOU_{agc}^{orig}	69.9	72.8	58.4	100.0	62.2	49.4	62.8	47.2	54.7	49.4
4	PGD-AT	IOU_{agc}^{adv}	86.0	80.2	91.3	84.7	100.0	76.1	91.3	74.4	84.1	78.2
		IOU_{agc}^{orig}	80.9	74.5	89.8	79.7	100.0	68.0	87.9	67.1	78.0	72.5
	STD-TR	IOU_{agc}^{adv}	76.9	71.1	86.3	75.4	100.0	66.4	83.5	65.4	76.1	69.0
		IOU_{agc}^{orig}	65.4	55.1	81.0	62.2	100.0	48.9	79.4	46.0	64.9	54.8

Table 8: CONV DLGN -N128-D4 PGD-AT vs STD-TR model IOU of active gate count between class-pairs over adversarial and original examples for Fashion MNIST dataset.

Src Class	Train Type	Quantity	Class 0	Class 1	Class 2	Class 3	Class 4	Class 5	Class 6	Class 7	Class 8	Class 9
0	PGD-AT	IOU_{agc}^{adv}	100	70.2	83	82.7	81.8	83.9	82.7	77.4	84	80.6
		IOU_{agc}^{orig}	100	66.2	79.3	79.4	77.9	81.3	78.5	72.7	81.2	76
	STD-TR	IOU_{agc}^{adv}	100	78.1	84.7	82	81	84.5	84	80	78.2	82.6
		IOU_{agc}^{orig}	100	59.7	74.7	75	73.1	77.6	73.2	66.2	77.5	69.7
1	PGD-AT	IOU_{agc}^{adv}	70.2	100	74.9	75.8	74.7	74.2	75	77.2	76.3	75.6
		IOU_{agc}^{orig}	66.2	100	71.9	74.3	71.9	71	71.6	75	74.2	73.6
	STD-TR	IOU_{agc}^{adv}	78.1	100	82.7	79.5	80	80	79.3	83.3	74.9	80.4
		IOU_{agc}^{orig}	59.7	100	63.7	66.5	65.6	64.4	64.7	67.4	68.4	67.2
2	PGD-AT	IOU_{agc}^{adv}	83	74.9	100	86.9	84.3	83.5	85.8	79.7	86.1	82.4
		IOU_{agc}^{orig}	79.3	71.9	100	84.7	80.5	80.1	82.7	74.9	83.4	78.3
	STD-TR	IOU_{agc}^{adv}	84.7	82.7	100	82.4	83.9	83.3	85.7	82	79.2	83
		IOU_{agc}^{orig}	74.7	63.7	100	80.7	74.2	74.9	77	68.2	77.5	70.5
3	PGD-AT	IOU_{agc}^{adv}	82.8	75.8	86.9	100	82.7	86.3	82.1	81.7	87.4	83
		IOU_{agc}^{orig}	79.4	74.3	84.7	100	78.6	84.7	78	77.8	85.4	79
	STD-TR	IOU_{agc}^{adv}	82	79.5	82.4	100	77.5	85.4	77.6	83.6	75.7	81.8
		IOU_{agc}^{orig}	75	66.5	80.7	100	73.4	80.8	72.3	71.9	81.4	73
4	PGD-AT	IOU_{agc}^{adv}	81.8	74.7	84.3	82.7	100	85.8	84.7	85.4	86.9	91.1
		IOU_{agc}^{orig}	77.9	71.9	80.5	78.6	100	82.3	81.3	82.8	84.5	90.6
	STD-TR	IOU_{agc}^{adv}	81	80.2	83.9	77.8	100	81.2	82.5	80.7	80.8	87.2
		IOU_{agc}^{orig}	73.1	65.6	74.2	73.4	100	78.5	75	77.7	80	85.9

Table 9: CONV DLGN -N128-D4 PGD-AT vs STD-TR model IOU of active gate count between class-pairs over adversarial and original examples in MNIST dataset.

MN Class (<i>c</i>)	PGD-AT <i>I^{org}</i>	PGD-AT <i>I^{adv}</i>	STD-TR <i>I^{org}</i>	STD-TR <i>I^{adv}</i>	Fashion MN (<i>c</i>)	PGD-AT <i>I^{org}</i>	PGD-AT <i>I^{adv}</i>	STD-TR <i>I^{org}</i>	STD-TR <i>I^{adv}</i>
0					Ankle-boot				
1					Bag				
2					Coat				
3					Dress				
4					Pullover				
5					Sandal				
6					Shirt				
7					Sneaker				
8					T-shirt				
9					Trouser				

Table 10: Image I which triggers dominating gating pattern per class obtained on adversarial examples (column 3,5,8,10) and original examples (column 2,4,7,9). Columns 2,3,7,8 are on the PGD-AT model, and columns 4,5,9,10 are on the STD-TR model. Loss function is as per Equation (6), $\lambda = 0.9$, $\alpha = 0.1$, optimization is as per Equation (7)

MN Class (<i>c</i>)	PGD-AT <i>I</i> _{ado}	PGD-AT <i>I</i> _{amo}	STD-TR <i>I</i> _{ado}	STD-TR <i>I</i> _{amo}	Fashion MN (<i>c</i>)	PGD-AT <i>I</i> _{ado}	PGD-AT <i>I</i> _{amo}	STD-TR <i>I</i> _{ado}	STD-TR <i>I</i> _{amo}
0					Ankle-boot				
1					Bag				
2					Coat				
3					Dress				
4					Pullover				
5					Sandal				
6					Shirt				
7					Sneaker				
8					T-shirt				
9					Trouser				

Table 11: Image I which triggers dominating active gating pattern per class obtained on adversarial examples alone but not on original examples (columns 2,4,7,9) and obtained both on original examples and adversarial examples (columns 3,5,8,10). Columns 2,3,7,8 are on the PGD-AT model, and columns 4,5,9,10 are on the STD-TR models. Loss function is as per Equation (6), $\lambda = 0.9$, $\alpha = 0.1$, optimization is as per Equation (7)